

Article

Experimental Study on the Streaming Potential Phenomenon Response to Compactness and Salinity in Soil–Rock Mixture

Xin Zhang ¹, Mingjie Zhao ¹ and Kui Wang ^{2,*}

¹ Key Laboratory of Hydraulic and Waterway Engineering of the Ministry of Education, Chongqing Jiaotong University, Chongqing 400074, China; zx@mails.cqjtu.edu.cn (X.Z.); 990000980717@cqjtu.edu.cn (M.Z.)

² Engineering Research Center of Diagnosis Technology and Instruments of Hydro-Construction, Chongqing Jiaotong University, Chongqing 400074, China

* Correspondence: 990201300054@cqjtu.edu.cn

Abstract: The study on the effect of material structure and solution properties on the streaming potential of the soil–rock mixture (SRM) will be beneficial for improving the reliability of the measurement results for self-potential monitoring in embankment dams. We design two experimental groups and investigate the changes of potential and pressure during seepage of SRM (slightly clay materials) with different compactness and different concentration. The effects of the compaction degree and solution concentration on the streaming potential coupling coefficient and streaming potential were analyzed. The test results demonstrate that when the clay content in soil matrix is slight, the potential has a linear relationship with the hydraulic head difference, and seepage obeys Darcy's law. The surface conductivity is negligible at 0.01 M (1 M corresponds to a concentration of 58.4 g L⁻¹) salinity, the compactness of the SRM decreases (the permeability coefficient increases), the apparent streaming potential coupling coefficient and pressure difference decrease is the reason streaming potential decreases. The permeability coefficient of the SRM is not affected by the change in salinity (0.0001–1 M) at 85% compactness, and its seepage characteristics are related to the mineral composition, morphology and the thickness of the bound water layer (electric double layer). This study lays a foundation for further research on the self-potential method to monitor the structure of embankment dams.

Keywords: soil–rock mixture (SRM); compactness; salinity; streaming potential coupling coefficient; streaming potential



Citation: Zhang, X.; Zhao, M.; Wang, K. Experimental Study on the Streaming Potential Phenomenon Response to Compactness and Salinity in Soil–Rock Mixture. *Water* **2021**, *13*, 2071. <https://doi.org/10.3390/w13152071>

Academic Editors: Jianchao Cai and Steffen Berg

Received: 26 June 2021

Accepted: 25 July 2021

Published: 29 July 2021

Publisher's Note: MDPI stays neutral with regard to jurisdictional claims in published maps and institutional affiliations.



Copyright: © 2021 by the authors. Licensee MDPI, Basel, Switzerland. This article is an open access article distributed under the terms and conditions of the Creative Commons Attribution (CC BY) license (<https://creativecommons.org/licenses/by/4.0/>).

1. Introduction

The charged porous media materials in contact with water form a double electric layer (stern layer and diffusion layer) at the solid–liquid interface. The counter ions in the stern layer are immobile, whereas the counter ions in the diffusion layer are mobile, and fluid flow drives the movement of excess cations in the diffusion layer to generate streaming potential [1]. There have been several studies on the streaming potential phenomenon of rock and soil; however, studies on the streaming potential of soil–rock mixture (SRM) as a type of composite porous medium material are still lacking. Owing to the substantial size difference between soil and rock, uneven spatial distribution, and clear differences in mechanical properties, it is difficult to study the seepage mechanism of the SRM [2,3]. The SRM is often used as a filling material for dams. Seepage characteristics, as the main engineering characteristics of SRMs, have always been the focus of dam safety monitoring. The streaming potential phenomenon is closely related to the seepage process, and by collecting the streaming potential signal, we can capture the water flow information in real time [4–6]. Therefore, it is of great theoretical significance and engineering application value to conduct a study on the streaming potential phenomena of SRM to further explore

the seepage mechanism of SRM, and to establish a long-term seepage stability evaluation system for embankment dams.

The streaming potential coupling coefficient is a key physical parameter that characterizes the coupled hydroelectric problem of porous material. The following is the classical Helmholtz–Smoluchowski (HS) Equation (1) that is used to calculate the streaming potential coupling coefficient [7,8]:

$$C = \frac{\varepsilon\zeta}{\mu\sigma_f} \quad (1)$$

where ε (F m^{-1}) is the dielectric permittivity, μ (Pa s) is the dynamic viscosity, σ_f (S m^{-1}) is the fluid conductivity, ζ (V) is the zeta potential. The zeta potential is the potential in the shear plane that controls the ion distribution within the diffusion layer. Factors found to be influencing coupling coefficient and zeta potential have been explored in several studies as follows.

A significant number of different porous materials (sandstone, sand, granite, and basalt) use different concentrations of NaCl solutions as flowing fluids. The streaming potential response law in the flow process was recorded in the laboratory. The test results demonstrate that the streaming potential coupling coefficient decreases with an increase in concentration at low salinity, because of the decreasing zeta potential [9–12]. At high salinity, the streaming potential coupling coefficient did not reduce to 0, and the zeta potential remained a constant. Jaafar et al. [13] and Vinogradov et al. [14] attribute this to the thickness of the Debye length that is the same as the hydrated sodium ion diameter. Walker and Glover [15] measured a large amount of high-quality streaming potential coupling coefficient and zeta potential data using a self-designed device [16], and found the same phenomenon in the solution concentration variation range 10^{-5} –4.5 M. Similar test results can also be obtained for different concentrations of KCl [17–19].

In porous media containing clay minerals, salinity variations affect not only the magnitude of zeta potential, but also the permeability. Solution salinity controls the stability of clay minerals. Low salinity solutions are prone to dispersion due to their inability to counteract the negative charge on the surface of the clay particles, and block the pore throat, reducing the permeability of porous media. Clay particles are relatively stable at high salinity, resulting in a higher permeability of porous media [20,21]. The change of concentration will lead to the change of pore size distribution, which controls the permeability of porous media [22]. Some scholars equate the thickness of the electric double layer to the thickness of the bound water layer, and the electric double layer is related to the Debye length. Therefore, the thickness of the Debye length can be compared with the pore radius to evaluate the effect of the change of solution concentration on the permeability of clay materials [23,24].

The HS equation (Equation (1)) is valid when the surface conductivity is neglected. However, surface conductivity plays an important role in transporting ions at low concentration and low permeability. The permeability of sandstone and limestone is directly proportional to the coupling coefficient, and the dependence decreases with the increase in concentration [25]. Jouniaux and Pozzi [26] have studied the relationship between the structure of porous media and the streaming potential coupling coefficient by considering the surface conductivity into the HS equation:

$$C = \frac{\varepsilon\zeta}{\mu(\sigma_f + \sigma_s)} = \frac{\varepsilon\zeta}{\mu\sigma_{rw}F} \quad (2)$$

where σ_s (S m^{-1}) is the surface conductivity, σ_{rw} (S m^{-1}) is the electrical conductivity of the saturated sample, F is the intrinsic formation factor of the sample. Further research found that the streaming potential coupling coefficient was mainly affected by the comprehensive influence of the microstructural parameters (porosity, particle size, and formation factor) at low salinity [27]. However, the zeta potential is independent of the structure of the porous medium [28].

Another option to take into account the effect of surface conductivity on the coupling coefficient is the effective excess charge approach. The basic idea of this approach is to use the effective excess charge in the diffusion layer to be dragged by the water flow to explain the generation of streaming potential, and the quantitative relationship between the coupling coefficient and the effective excess charge density is established [29,30]:

$$C = -\frac{\hat{Q}_v k}{\mu \sigma} = -\frac{\hat{Q}_v k F}{\mu(\sigma_f + \sigma_s)} \quad (3)$$

where \hat{Q}_v (C m^{-3}) is the effective excess charge density, k (m^2) is the permeability, σ (S m^{-1}) is the electrical conductivity of the medium. The effects of the structure of the medium and surface conductivity are included in the relationships obtained in the effective excess charge approach [31]. As an analytical model of the effective excess charge density is proposed by Guarracino and Jougnot [32], the relationship between effective excess charge density and permeability, porosity, concentration, and the zeta potential are revealed, and the use of effective excess charge approach became more convenient.

The above analysis verifies that the medium structure and solution concentration have been considered as the main factors of the streaming potential phenomenon. However, the influence of structure and solution concentration on the streaming potential effect of SRM has not been systematically analyzed, and its mechanism is still poorly understood.

Electrical resistivity tomography (ERT) and self-potential method are commonly used in geophysical exploration. ERT measurement needs to provide power, the resistivity distribution is obtained by inversion, and the underground structure is identified according to the difference in resistivity [33]. ERT has a good performance in detecting water content distribution and saturation of medium [34], but it takes a certain time to scan one section each time, which is unfavorable for monitoring the seepage with high velocity. In addition, soil water salinity affects soil conductivity and makes it difficult to identify preferential paths [35]. The self-potential method using non-polarizable electrodes is a passive monitoring method. This method measures the electric field generated by the water flow process and identifies the groundwater flow patterns based on distribution characteristics of self-potential signals. It is an ideal tool for monitoring water flow and salt tracer transport in real time, and estimating flow velocity and media permeability [36,37].

Due to the advantage of the self-potential method of monitoring water flow patterns at a distance without providing power, some scholars have applied it in the localization of leakage of embankment dams and their quantitative analysis. Panthulu et al. [38] combined the resistivity and self-potential methods to delineate the leakage path in an earth rock dam and they analyzed the corresponding relationship between the seepage rate and self-potential anomaly. Sheffer and Oldenburg [39] established a three-dimensional finite volume algorithm to calculate the self-potential, and the results obtained from calculating the electric field of earth rock dams with leakage were consistent with the measured self-potential data. Bolève et al. [40] realized the location of the leakage by monitoring the movement of the salt tracer in the embankment dam using the self-potential method, and quantitatively analyzed the permeability of the leakage. The effectiveness of the self-potential method was verified through laboratory and field tests. Soueid Ahmed et al. [41,42] analyzed the influence law of leakage flow pattern and material on the self-potential distribution through numerical simulation, and the reliability of the numerical simulation was verified by monitoring the self-potential of the leakage path at different water levels through model tests. On this basis, the permeability of the leakage channel was further quantified through numerical simulations and field tests using the stochastic inversion theory.

At present, the leakage detection technology of embankment dams has matured gradually, and this can not only delineate the location of the leakage but also quantitatively analyze the physical parameters of the leakage. However, we are more interested in monitoring the structural evolution of dams during operation in engineering, which is beneficial for dam safety assessment and early warning. Accordingly, we designed five compaction degrees of 75%, 80%, 85%, 90%, and 95%, representing five different structures

of SRM, and we collected potential and pressure data in 0.01 M NaCl solution to study the response characteristics of the streaming potential coupling coefficient under different structures. In addition, there are few reports on the influence of the change of solution concentration on the streaming potential effect and seepage of the SRM. Therefore, we recorded the potential and pressure in 0.0001, 0.001, 0.01, 0.1, and 1 M NaCl solutions with 85% compaction, and studied the constraint law of streaming potential coupling coefficient at different concentrations. In this study, we aim to: (i) explore the streaming potential phenomenon of an SRM, (ii) clarify the restriction law of compaction and concentration on the streaming potential phenomenon of the SRM, and (iii) promote the application of the self-potential method for dam structure monitoring.

2. Apparatus and Methodology

2.1. Apparatus

The new apparatus is illustrated in Figure 1. It is mainly composed of a water tank, polyvinyl chloride (PVC) pipe, and an acquisition system. The water tank was made of plexiglass, and two plexiglass plates with holes were used in the middle to form a $400 \times 200 \times 200$ mm SRM filling area. A nylon net was placed between the SRM and the plexiglass plate to prevent fine particle loss. The upstream side of the tank was connected to the PVC pipe, whereas the downstream side was the seepage outlet.

We directly compacted the SRM in the water tank and prevented leakage near the wall by using the squeezing action produced during the compaction process [43]. The height of the sample is flush with the water tank, and a thin layer of fine particle is spread on the sample. A piece of compressible and impermeable foam with a thickness of 3 mm was placed on top of the fine particle. When the roof of the tank was fixed with bolts and nuts, it exerted pressure on the foam and prevented water from flowing away from the top. To ensure sealing of the roof and water tank, a rubber was placed between them.

The data acquisition system consists of sensor and acquisition instrument. During the compaction of the SRM, two CYG1145 pressure sensors (Baoji Qinming Sensor Co., Ltd., Baoji, China) (with measurement range from -50 to 50 kPa and an accuracy grade of 0.5) were installed, and the distance between two pressure sensors was 20 cm. The outer part was connected to a DH3821 pressure acquisition instrument (Jiangsu Donghua Testing Technology Co., Ltd., Jingjiang, China) (with measurement range from -5000 to 5000 mV, accuracy 0.1%, and frequency of measurement 2 Hz). The pressure acquisition instrument could be automatically controlled using a computer. The pressure sensor must be calibrated at five points before each experiment to ensure measurement accuracy. The Ag/AgCl non-polarizable electrodes were inserted into the SRM through the reserved position of the customized mold. The reference electrode was on the downstream side, whereas the electrode and pressure sensor were in the same cross-section. The non-polarizable electrode was placed in a chamber filled with saturated KCl solution. To alleviate diffusion effects, the surface area of the electrode chamber contacted with the saturated porous medium was reduced (see Figure 1b). In addition, the porous ceramic contacted with medium was helpful to reduce electrode leakage. Therefore, the electrode effect in the measurement was limited [44]. The potential acquisition was completed by a DM3058 multi-function digital multimeter (RIGOL, Suzhou, China) (with measurement range from 200 mV to 1000 V, resolution 0.001 mV, accuracy 0.1%, and frequency of measurement 2 Hz). Upstream and downstream Ag/AgCl non-polarizable electrodes were connected to the positive and negative terminals of the multi-function digital multimeter, respectively. The water content sensor (with a measurement accuracy of 2% and measurement range 0–100%) was used to monitor the saturation of the cross section where the pressure sensor and electrode were located.

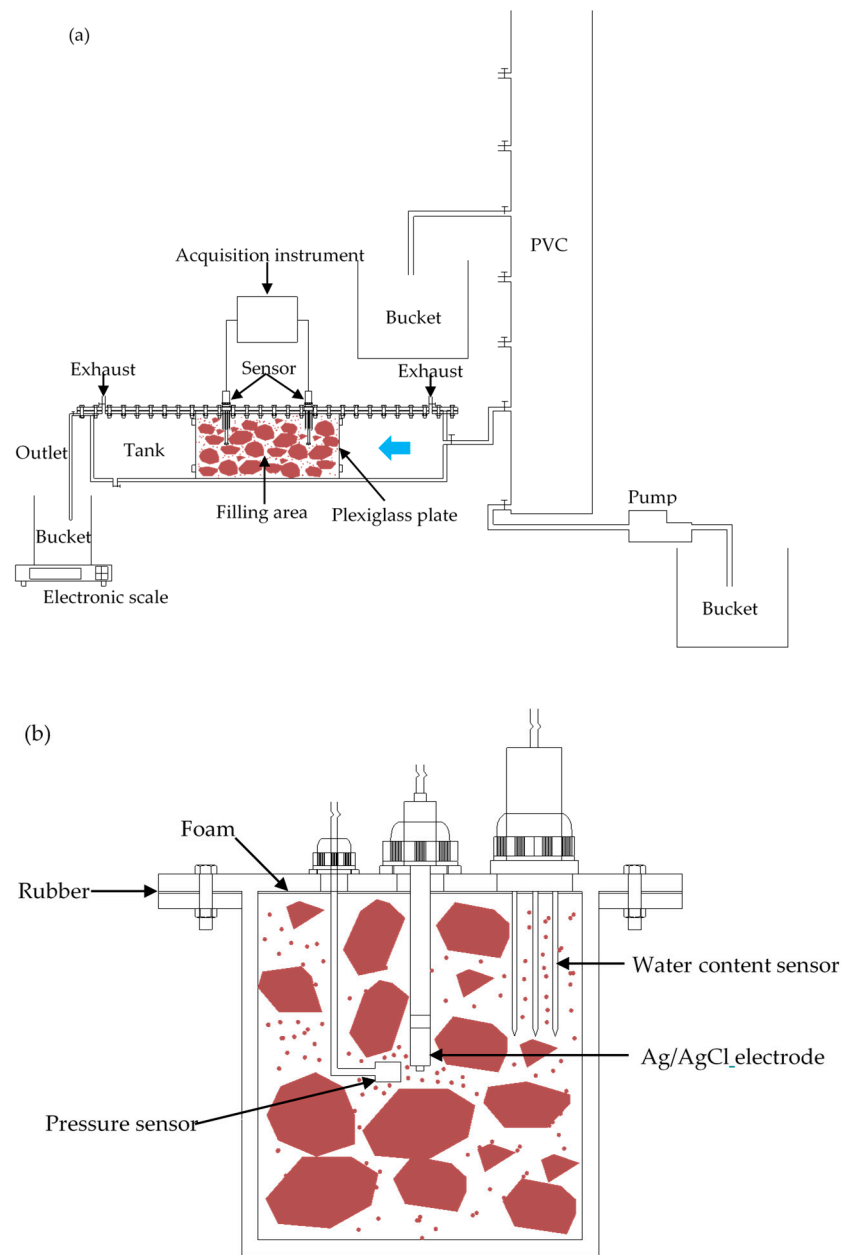


Figure 1. Sketch of the experimental apparatus. (a) The apparatus consists of tank (filling area, plexiglass plate, exhaust, outlet), PVC pipe (pump, bucket), and data acquisition system (sensor and acquisition instrument), the blue arrow represents the direction of the water flow. (b) Cross section through the sensor (water content sensor, Ag/AgCl non-polarizable electrode, pressure sensor, rubber, foam).

The PVC pipe was used to control the hydraulic head. There were a total of 5 water levels that were spaced at 20 cm. The flow-adjustable pump continuously supplied water to the PVC pipe during the measurement process, and the excess water in the PVC pipe was collected through a bucket to ensure a stable water level. The two exhaust ports on the top plate were opened during the saturation process and subsequently closed when the saturation was complete. The seepage flow rate was obtained by weighing the mass of the solution during a specific period of time using an electronic scale.

2.2. Material Design and Preparation

The material of the SRM is weathered broken argillaceous rock with a maximum particle size of 60 mm, natural water content of 2.57%, and specific gravity of 2.72. To prevent the emergence of oversized soil, the maximum particle size should be less than 10 times the width of the water tank [45]; therefore, the maximum particle size of the material is less than 20 mm after sieving (see Figure 2a). In this paper, the threshold value of soil and rock is referred to the 5 mm adopted by Zhou et al. [45], that is, more than 5 mm is rock and less than 5 mm is soil. The gradation curve designed in this experiment is shown in Figure 2b, along with the content of each particle size: 20–10 mm (12%), 10–5 mm (18%), 5–2 mm (22%), 2–1 mm (16%), 1–0.5 mm (11%), 0.5–0.25 mm (9%), 0.25–0.075 mm (9%), and <0.075 (3%). The same grading curve was adopted for SRMs with different compactness. The nonuniform coefficient C_u (a factor reflecting the degree of uniformity of particle gradation in the soil) is obtained from the following equation [46]:

$$C_u = \frac{d_{60}}{d_{10}} \quad (4)$$

where d_{10} (mm) and d_{60} (mm) denote the particle sizes of 10% and 60% of the total mass on the particle size distribution curve, respectively. The curvature coefficient C_c (the shape of the particle size distribution curve is a factor reflecting the degree of superiority of particle grading) can be obtained from the following equation:

$$C_c = \frac{d_{30}^2}{d_{10} \cdot d_{60}} \quad (5)$$

where d_{30} denotes the particle size of 30% of the total mass on the particle size distribution curve. To avoid piping during the test, we calculated C_u and C_c values to determine the gradation characteristics of the soil. $C_u = 16.5$ and $C_c = 1.23$. $C_u \geq 5$ and $C_c = 1-3$ are considered to be well-graded soils [47]. Figure 3a shows the SEM image of argillaceous particles surface. We found that the surface of the particles had an irregular scaly stacking structure, with slight alterations at the edges, and a small number of suspected holes after local amplification. We obtained the mineralogy of the rock using X-ray diffraction (see Figure 3b). The mineral composition of the argillaceous rock was quartz (48.8%), illite (22%), albite (17.9%), kaolinite (2.7%), chlorite (5.5%), calcite (1.8%), and hematite (1.2%).

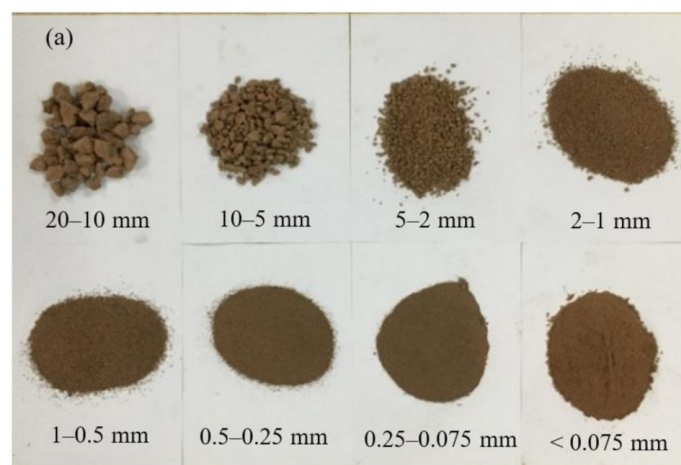


Figure 2. Cont.

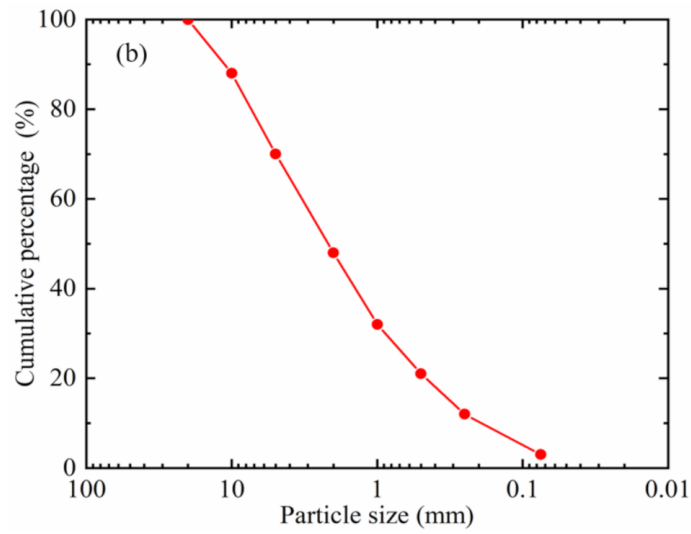


Figure 2. Particle characteristics. (a) Photograph of the particle size. (b) Cumulative gradation curve.

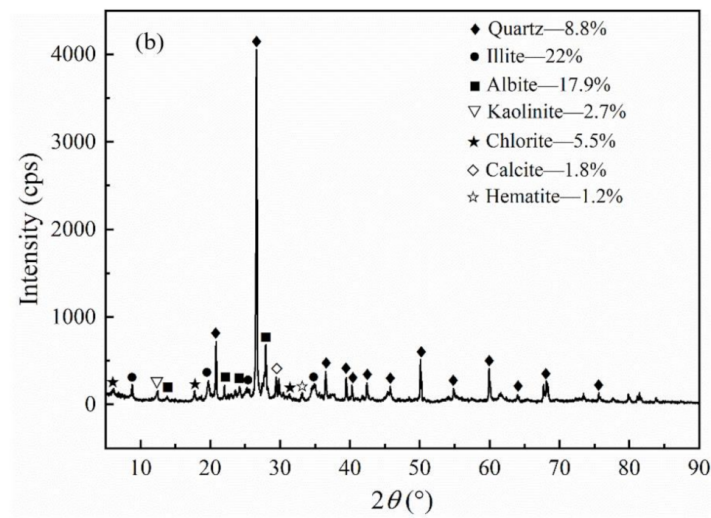
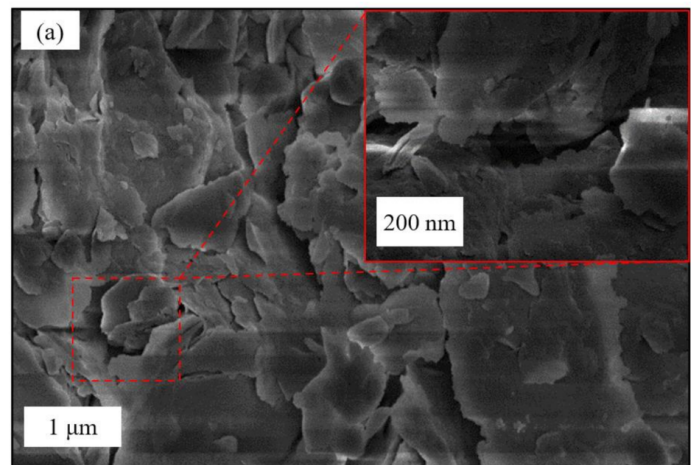


Figure 3. Material properties. (a) SEM images of particles surface. The inset focusing on the pore domain. (b) Mineral intensity versus 2θ , obtained from X-ray diffraction of the weathered broken argillaceous rock.

In accordance with the purpose of this experiment, a specific experimental scheme design is summarized in Table 1. We used the following steps to prepare samples with different compactness. The maximum dry density $\rho_d = 2.18 \text{ (g cm}^{-3}\text{)}$ and optimal moisture content $w = 5.6\%$ were obtained through a compaction experiment. Thereafter, according to the compactness (75%, 80%, 85%, 90%, and 95%), the mass of SRM required for each group of experiments was calculated. Second, the SRM was mixed with water at the optimal moisture content after drying. Finally, we sealed it with plastic wrap and let it stand for one day, as shown in Figure 4a. We compact the SRM into two layers, each of which is 10 cm thick. The degree of compaction is controlled by the quality of the SRM.

Table 1. Experimental scheme.

Grouping Scheme	Compactness (%)	Concentration (M)
A1–A5	75, 80, 85, 90, 95	0.01
B1–B5	85	0.0001, 0.001, 0.01, 0.1, 1

A1–A5 represents compactness 75, 80, 85, 90, 95%. B1–B5 represents the concentration of NaCl solution 0.0001, 0.001, 0.01, 0.1, 1 M. A3 and B3 are the same conditions.

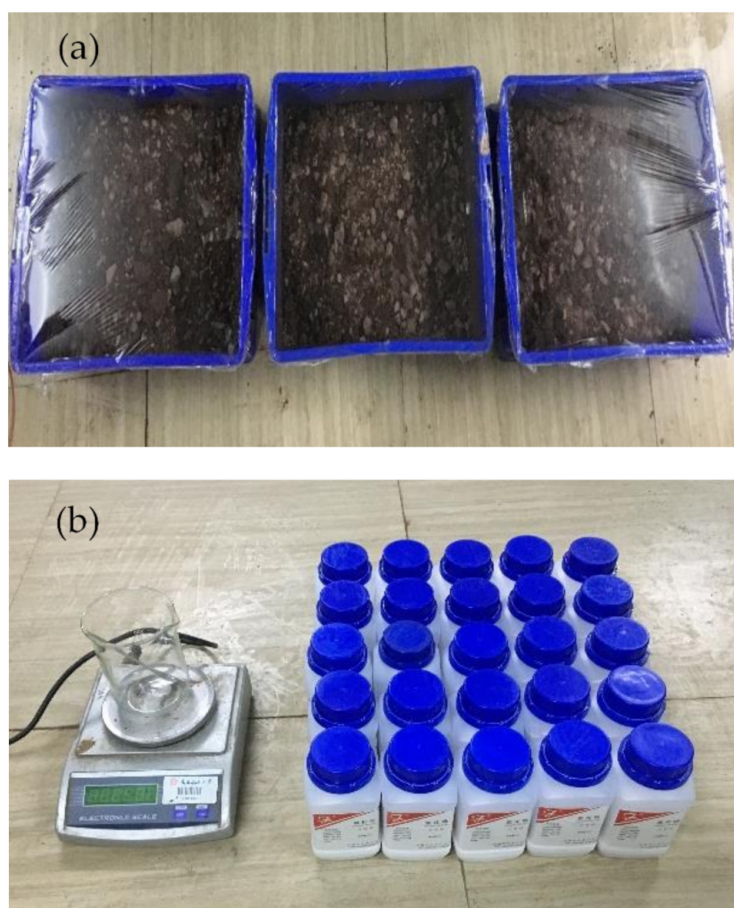


Figure 4. Preparation of SRM and solution. (a) SRM mixed with water and sealed. (b) NaCl white crystalline material.

In the experiment of SRM with different solution concentrations, we designed five concentrations (0.0001, 0.001, 0.01, 0.1, and 1 M) of NaCl solution. The mass of NaCl and the volume of deionized water were calculated. A NaCl white crystalline material with 99.5% purity was used in the experiment (as shown in Figure 4b). CJ-CS-K03 automatic ultra-pure water equipment (Dongguan sibaikang Environmental Protection Technology Co., Ltd., Dongguan, China) provided deionized water for this test and monitored its

conductivity during the preparation of the solution. After compacting the SRM in the water tank, it was left in the NaCl solution until the upstream and downstream equilibrium were achieved. The pH value of the solution was measured using an AZ-86031 multifunctional water quality detector (AZ Instrument Corp., Taiwan, China) (measurement range: 2–12, accuracy: ± 0.1 , resolution: 0.1) at 0.0001 – 0.1 M salinity and the PHS-25 pH meter (Shanghai INESA Scientific Instrument Co., Ltd., Shanghai, China) (measurement range: 0.00–14.00, accuracy: ± 0.05 , resolution: 0.01) at 1 M salinity, respectively. In the test where the degree of compaction is 75–95%, we measured the pH values as 7.3 ± 0.2 , 7.5 ± 0.1 , 7.5 ± 0.3 , 7.5 ± 0.2 , and 7.6 ± 0.3 , respectively. In the test with salinity ranging from 0.0001 to 1 M, we measured the pH values as 7.6 ± 0.2 , 7.4 ± 0.3 , 7.5 ± 0.3 , 7.3 ± 0.3 , and 7.2 ± 0.1 , respectively.

2.3. Test Procedure

We measured the potential of SRM ψ_0 (mV) at rest before each test. After the potential was stable, the hydraulic head was suddenly applied to the upstream water tank. The potential ψ_1 (mV) and hydraulic head difference H (cm) during flow were measured. The streaming potential ΔU (mV) is obtained using Equation (6) in the steady state as follows:

$$\Delta U = \psi_1 - \psi_0 \quad (6)$$

Thereafter, the second to fifth hydraulic heads were measured. It is difficult to measure streaming potential at high salinity ($C_f > 0.01$ M), although the resolution of the instrument reaches 0.001 mV. To reduce the influence of static potential fluctuation on the potential at the steady state, we adopted the following measures: preheat the instrument for half an hour before measurement; turn off other electronic devices; perform grounding tests on all instruments. Each group of experiments (A1–A5, B1–B5) followed the test protocol described above. The streaming potential coupling coefficient is given by the slope of the linear regression of streaming potential ∇U (mV) against the hydraulic head difference ∇H (cm) [48].

The volume of water over a period of time was recorded. The permeability coefficient is calculated using Darcy's law [46] as follows:

$$K = \frac{QL}{AHt} \quad (7)$$

where K (cm s^{-1}) is the permeability coefficient, Q (cm^3) is the volume of water, L (cm) is the sample length, A (cm^2) is the sample cross-sectional area, H (cm) is the hydraulic head difference, t (s) is the test time.

In the same conditions, we measured the electrical conductivity of SRM separately. The stainless-steel electrode network was arranged at both ends of the SRM, saturated in solution until the solution equilibrium at both ends, and the resistance of the SRM is measured using a two-electrode device of DM3058 multi-function digital multimeter. In addition, we measured the electrical conductivity of SRM in 1 M solution at different compactness. The conductivity of the solution was measured by DDS-307 (Shanghai INESA Scientific Instrument Co., Ltd., Shanghai, China) (with measurement range from 0.00 $\mu\text{S cm}^{-1}$ to 100 mS cm^{-1} and accuracy $\pm 1.0\%$ FS). We used the Olhoeft's equation to calculate the relative permittivity (Olhoeft, unpublished note, 1980) [27,49]:

$$\varepsilon_r(T, C_f) = a_0 + a_1T + a_2T^2 + a_3T^3 + c_1C_f + c_2C_f^2 + c_3C_f^3 \quad (8)$$

where $a_0 = 295.68$, $a_1 = -1.2283$ (K^{-1}), $a_2 = 2.094 \times 10^{-3}$ (K^{-2}), $a_3 = -1.41 \times 10^{-6}$ (K^{-3}), $c_1 = -13.00$ (L mol^{-1}), $c_2 = 1.065$ (L mol^{-1})², $c_3 = -0.03006$ (L mol^{-1})³, C_f (L mol^{-1}) is the salinity, T (K) is the Kelvin temperature. The Equation (8) is applicable from 273 to 373 K. The Dynamic viscosity was determined by the Phillips et al. [50] equation [27]:

$$\mu(T, C_f) = e_1 + e_2 \exp(\alpha_1 T) + e_3 \exp(\alpha_2 C_f^m) + e_4 \exp(\alpha_3 T + \alpha_4 C_f^m) \quad (9)$$

where $e_1 = 4.95166 \times 10^{-5}$ (Pa s), $e_2 = 6.034658 \times 10^{-4}$ (Pa s), $e_3 = 9.703832 \times 10^{-5}$ (Pa s), $e_4 = 1.025107 \times 10^{-3}$ (Pa s), $\alpha_1 = -0.06653081$ ($^{\circ}\text{C}^{-1}$), $\alpha_2 = 0.1447269$ (molal $^{-1}$), $\alpha_3 = -0.02062455$ ($^{\circ}\text{C}^{-1}$), $\alpha_4 = 0.1301095$ (molal $^{-1}$), T ($^{\circ}\text{C}$) is the Celsius degree, C_f^m (molal $^{-1}$) is the molality. Because the C_f and C_f^m are very close in the concentration range of 0.0001 to 1 M, here we take $C_f = C_f^m$. The properties of SRM are reported in Tables 2 and 3.

Table 2. Properties of SRM with different compactness.

Compactness	75%	80%	85%	90%	95%
Porosity	0.38	0.34	0.30	0.26	0.22
Temperature ($^{\circ}\text{C}$)	25	22	23	24	21
Electrolyte conductivity (S m^{-1})	0.089	0.086	0.088	0.086	0.084
Sample conductivity (S m^{-1})	1.42×10^{-3}	1.36×10^{-3}	1.33×10^{-3}	1.25×10^{-3}	1.20×10^{-3}
Formation factor	63.73	64.22	67.02	69.71	71.33
Dynamic viscosity (Pa s)	8.74×10^{-4}	9.38×10^{-4}	9.16×10^{-4}	8.95×10^{-4}	9.62×10^{-4}
Relative permittivity	78	79	79	79	80
Zeta potential (mV)	-62.01	-68.98	-74.92	-81.98	-89.67
Surface conductivity (S m^{-1})	1.23×10^{-3}	1.60×10^{-3}	1.25×10^{-3}	1.33×10^{-3}	1.45×10^{-3}
Coupling coefficient (mV cm^{-1})	-0.0543	-0.0587	-0.0641	-0.0734	-0.0773

Table 3. Properties of SRM with different concentrations.

Concentration	0.0001 M	0.001 M	0.01 M	0.1 M	1 M
Porosity	0.30	0.30	0.30	0.30	0.30
Temperature ($^{\circ}\text{C}$)	25	23	23	24	25
Electrolyte conductivity (S m^{-1})	0.0028	0.013	0.088	0.997	8.135
Sample conductivity (S m^{-1})	1.02×10^{-3}	1.10×10^{-3}	1.33×10^{-3}	1.49×10^{-2}	1.21×10^{-1}
Formation factor	67.02	67.02	67.02	67.02	67.02
Dynamic viscosity (Pa s)	8.73×10^{-4}	9.15×10^{-4}	9.16×10^{-4}	9.03×10^{-4}	9.73×10^{-4}
Relative permittivity	78	79	79	77	66
Zeta potential (mV)	-112.32	-105.86	-74.92	-67.43	N/A
Coupling coefficient (mV cm^{-1})	-0.1306	-0.1093	-0.0641	-0.0051	N/A

3. Results

3.1. Potential of SRM Changes with Pressure

Figure 5 shows the typical changes in the potential and hydraulic head difference at a concentration of 0.01 M and compactness of 85%. When the water is stationary, the hydraulic head difference and voltage fluctuate slightly. The hydraulic head difference increases rapidly after water is suddenly injected into the water tank, and it thereafter becomes stable, but it still fluctuates slightly with time. The variation in the potential is consistent with the hydraulic head difference.

3.2. Influence of Compactness on Streaming Potential Phenomenon

The streaming potential is calculated using Equation (6). Figure 6a shows the linear relationship between the streaming potential and hydraulic head difference. The streaming potential decreases with the decrease in compactness. The rate of decrease rapidly rises, particularly when the compactness decreases by more than 85%. The streaming potential coupling coefficient for different compaction degrees was obtained using the slope of the linear regression (see Figure 6b). The streaming potential coupling coefficient increases gradually with an increase in compactness, but the variable amplitude of the streaming potential coupling coefficient is small. The streaming potential coupling coefficient increases with a decrease in the permeability. The zeta potential is obtained from Equation (2). Table 2 shows that the zeta potential increases with the increase in compactness.

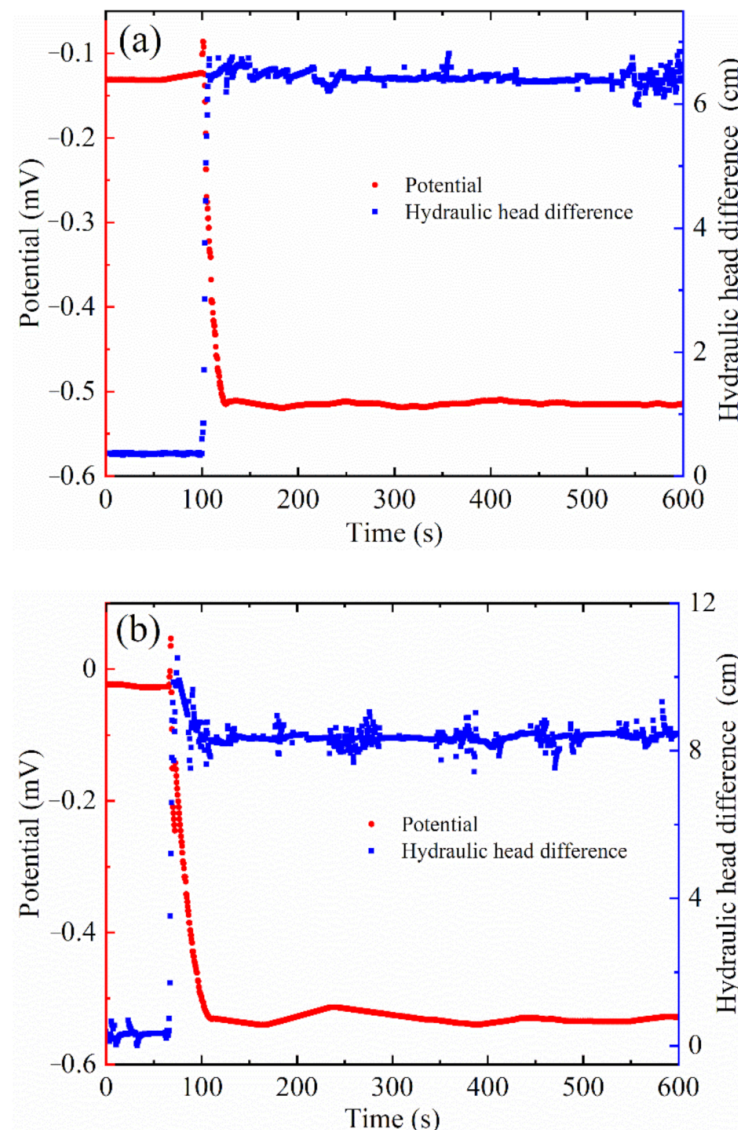


Figure 5. The change of potential and hydraulic head difference at different water levels when the compactness is 85% and the concentration is 0.01 M. (a) 20 cm hydraulic head. (b) 40 cm hydraulic head. The red circle symbols represent the potential, and the blue square symbols represent the hydraulic head difference.

3.3. Influence of Salinity on Streaming Potential Phenomenon

Figure 7 shows the variation in the streaming potential coupling coefficient and permeability coefficient for different salinities. The streaming potential coupling coefficient decreased with an increase in the solution concentration, which is consistent with previous studies [15]. We compare the distribution range of the streaming potential coupling coefficient with different salinities, which is consistent with the range of slightly clay materials predicted by Glover et al. [51]. The zeta potential is obtained from Equation (2). Table 3 shows that zeta potential decreased with the increase in concentration, except at a concentration of 1 M. Since the streaming potential values are very small at high concentrations, our instruments do not meet the resolution and accuracy requirements. In addition, the stability of the pore fluid is difficult to guarantee in SRM [13,14]. These two reasons lead to a large error in the measurement of the streaming potential coupling coefficient and propagate to the zeta potential. The change in concentration had no significant effect on the permeability coefficient.

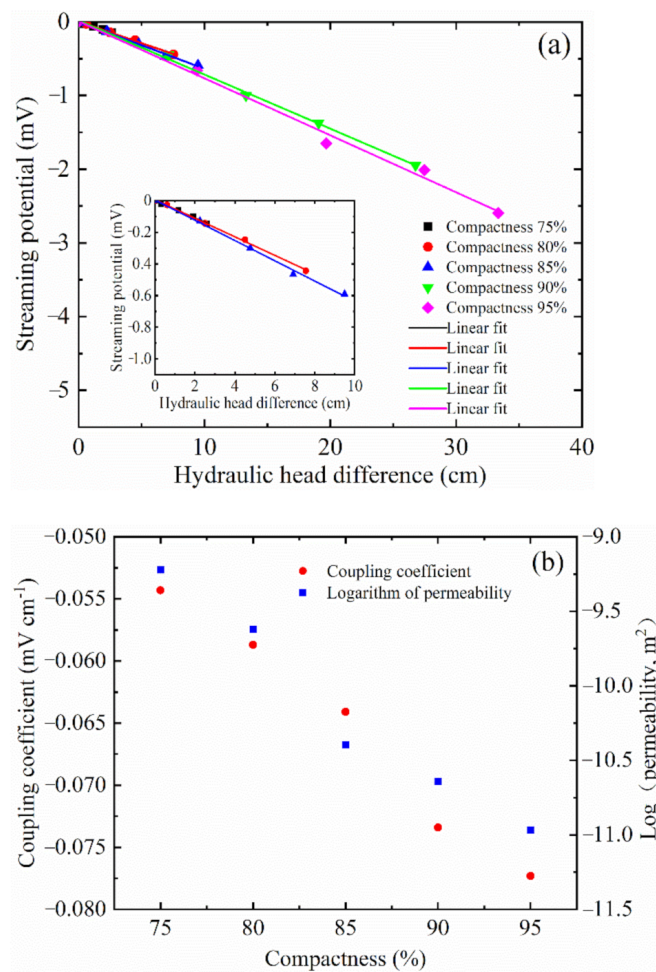


Figure 6. Experimental results of compactness. (a) Streaming potential ΔU (mV) against hydraulic head difference H (cm) for different compactness samples saturated with 0.01 M NaCl solution. The streaming potential coupling coefficient is determined as the slope of the linear regression. The inset focusing on the 75%, 80%, and 85% compactness domain. (b) The relationship between the coupling coefficient and permeability of SRM at different compactness.

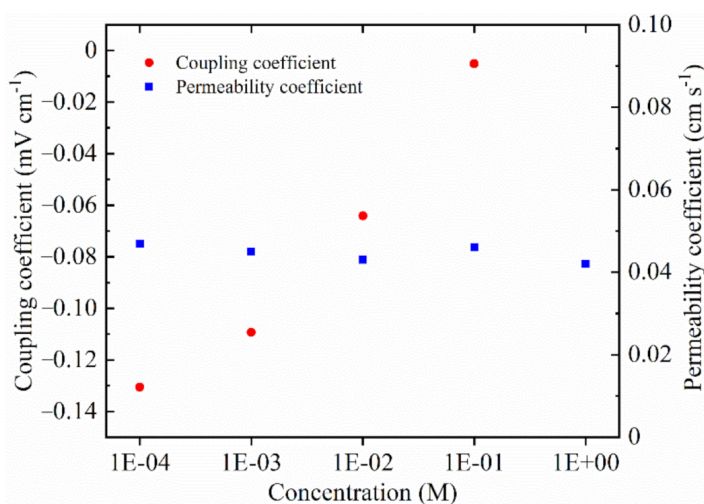


Figure 7. The relationship between the coupling coefficient and permeability coefficient of SRM at different concentration. The streaming potential coupling coefficient is equal to the slope of the linear regression.

3.4. Influence of Compactness and Salinity on the Effective Excess Charge Density

The effective excess charge density is determined by Equation (3). We obtained the relationship between the effective excess charge density and the compaction degree and concentration by power law fitting (see Figure 8). The effective excess charge density increases with the increase in compactness and decreases with the increase in concentration. The feature of these fits can be described by the relationship, respectively:

$$\hat{Q}_v = 0.17643C_o^{14.82689} \quad (10)$$

$$\hat{Q}_v = 0.01401C^{-0.07811} \quad (11)$$

where the C_o is the compactness, the C (M) is the concentration. These regression matches the available data with $R^2 = 0.994$ and $R^2 = 0.921$, respectively. The high compactness yields the porosity is smaller, and the specific surface area of SRM increases, so the total amount of effective excess charge present in the pore space per unit pore volume increases. The high concentration solution causes a large number of ions to be adsorbed in the stern layer, and the ion concentration in the diffusion layer decreases, hence reducing the amount of effective excess charge. The effects of compactness and concentration on the effective excess charge density are consistent with the results in the literature [22].

3.5. Comparing the Measured and Predicted Effective Excess Charge Density

In this section, we test the effective excess charge density model proposed by Guaracino and Jougnot [32]. All parameters used for model calculation have been obtained, except for the tortuosity. The Windsauer et al. [52] model is used to calculate the tortuosity:

$$\tau = \sqrt{F\phi} \quad (12)$$

where the τ is the tortuosity, the ϕ is the porosity. Figure 9 shows that the tortuosity decreases with the increase in compactness. The difference of particle size is large and the spatial distribution is uneven, so the tortuosity of SRM is large. According to Equation (12), there is little difference between the formation factors, the magnitude of the tortuosity is determined by porosity and, hence, the tortuosity is larger when the compactness is low.

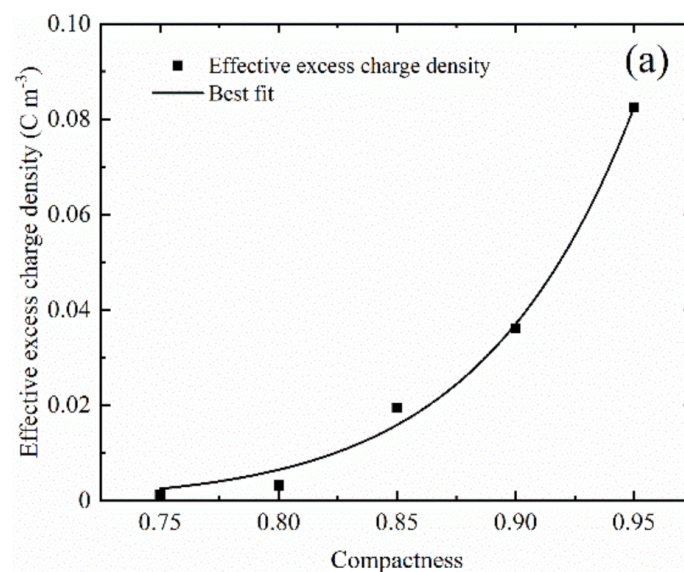


Figure 8. Cont.

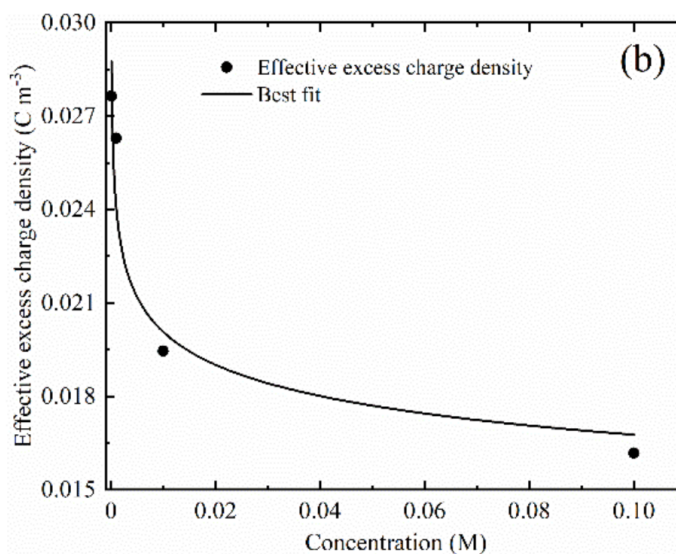


Figure 8. The empirical relationship between effective excess charge density and compactness and concentration. (a) The empirical relationship between effective excess charge density and compactness. (b) The empirical relationship between effective excess charge density and concentration.

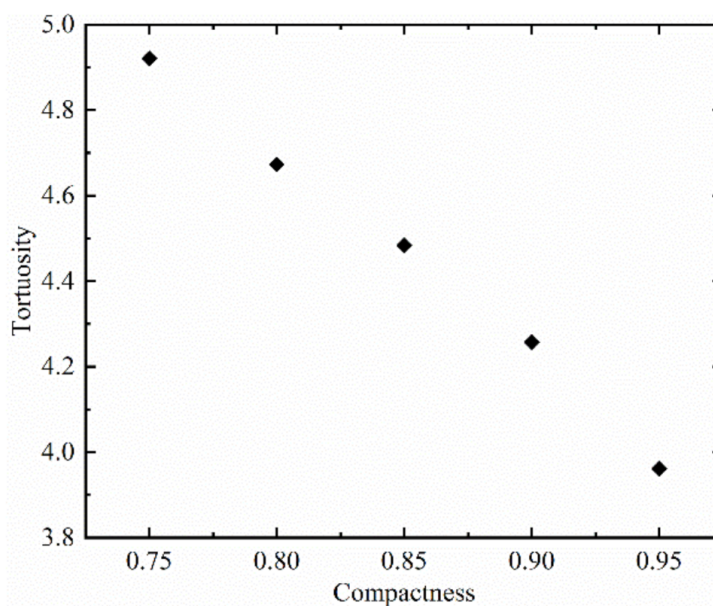


Figure 9. The evolution of the tortuosity with the compactness.

Figure 10 shows that the analytical model represents the experimental data very well when applied to the different compactness and different concentration. That is because Guarracino and Jougnot [32]’s model takes into account the fractal characteristics of the pore size distribution of porous media, and can accurately describe the feature of dual domain medium of SRM (permeability of rock and permeability that between soil particles) [53].

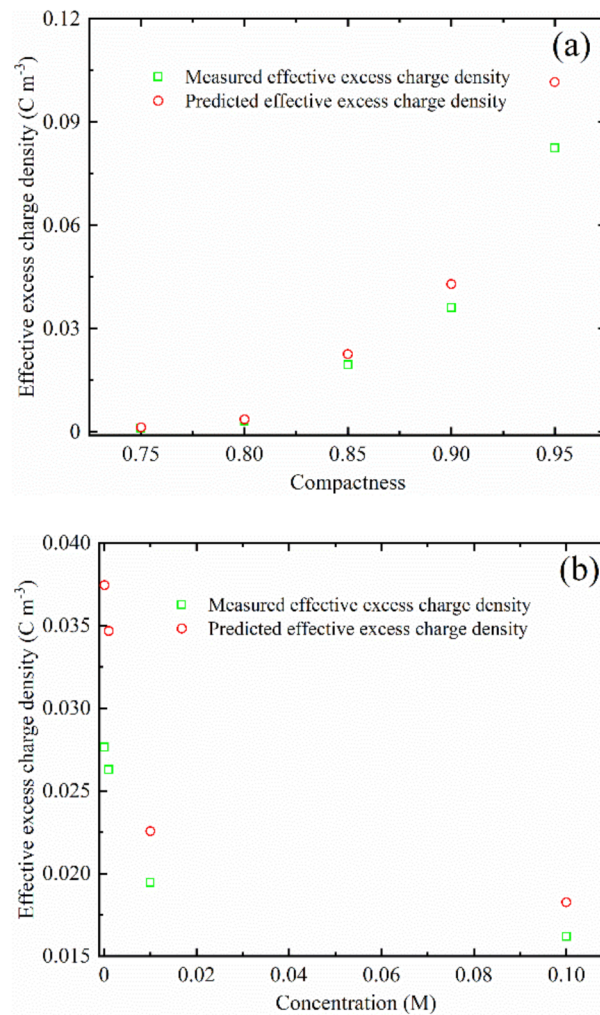


Figure 10. Comparing the measured the effective excess charge density with the predicted value by the model of Guarracino and Jougnot [32]. (a) The measured and predicted effective excess charge density with different compactness. (b) The measured and predicted effective excess charge density with different concentration.

4. Discussion

4.1. Streaming Potential Phenomenon in SRM

The streaming potential has a linear relationship with the hydraulic head difference, and the flow of SRM follows Darcy law. However, Wang et al. [54] found that the physical and mechanical properties of the soil matrix control the flow characteristics of the SRM. In his study, for the soil matrix with high clay mineral content (clay and mucky soil), the flow in the SRM follows the non-Darcy law, while the fine sand matrix follows the Darcy law. This implies that it may be necessary to use Forchheimer equation to characterize the seepage in the study of the streaming potential phenomenon of SRM with rich clay mineral soil matrices. The soil matrix of the SRM in our experiments had a higher silica content (48.8%) than the clay minerals (illite (22%), kaolinite (2.7%), and chlorite (5.5%)), this is the reason for following Darcy's law.

Clay–gravel mixture is generally used as the compacted impermeable material in the core wall of high embankment dams. When using numerical simulation methods to study the self-potential distribution of such dams, it is necessary to fully consider the seepage characteristics of the material, which may ensure the accuracy of numerical simulation and make a reasonable interpretation of the self-potential monitoring data.

4.2. Evolution with the Compactness

Streaming potential coupling coefficient and zeta potential is proportional to compactness in a 0.01 M solution. The relationship between streaming potential coupling coefficient and permeability (compactness) may be related to surface conductivity, which is determined from Equation (2) [25,27]. We compare surface conductivity with the conductivity of 0.01 M solution and find that surface conductivity is not important (see Table 2). Therefore, the dependence of the compaction on the streaming potential coupling coefficient is independent of the surface conductivity at salinity 0.01 M.

Several reports have shown that streaming potential coupling coefficient is affected by the flow state. In the viscous laminar flow regime, the streaming potential coupling coefficient is obtained by Equation (1). We calculate the minimum and maximum Reynolds number of the seepage process of SRM with different compactness. The Reynolds number is given by [46]:

$$\text{Re} = \frac{\rho_f U d_{50}}{\mu} \quad (13)$$

where ρ_f (kg m^{-3}) is the bulk density of the pore water, U (m s^{-1}) is seepage velocity, d_{50} is the particle sizes of 50% the total mass on the particle size distribution curve. Figure 11 shows that the Reynolds number decreases as the compactness increases, and the maximum Reynolds number exceeds 1 at both 75% and 80% compactness. The results show that the flow has transformed from viscous laminar flow to inertial laminar flow when the compaction is less than 85% [48]. This implies that the streaming potential has been deflected [55–57], which lead to a decrease in the slope of the regression line between the streaming potential and hydraulic head difference. Here, C is the measured apparent streaming potential coupling coefficient and ζ is the measured apparent zeta potential. Therefore, the apparent streaming potential coupling coefficient and apparent zeta potential decreases with the decrease in compactness.

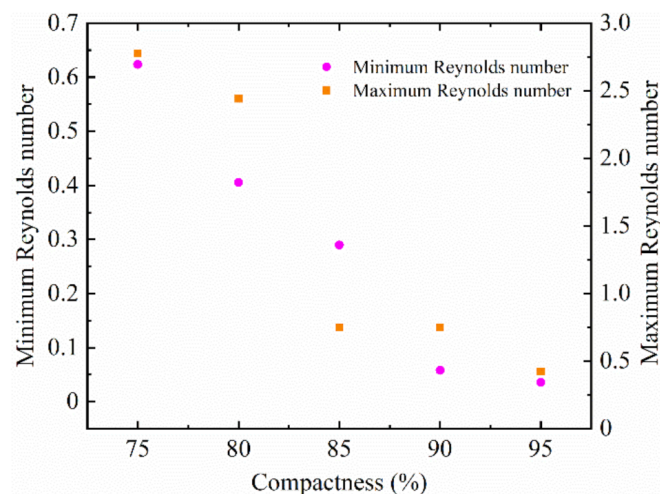


Figure 11. Minimum and maximum Rayleigh numbers of soil rock mixture with different compactness.

There is a correlation between the streaming potential coupling coefficient and the internal structure (compactness) of the SRM. The streaming potential changes significantly when the compaction degree is higher than 85%. That is because the streaming potential coupling coefficient and the hydraulic head difference increase at the same time. Changes in the streaming potential inevitably cause changes in the self-potential distribution. This means that we can monitor changes in the internal structure of embankment dams with the self-potential method. The self-potential method has the potential to monitor the occurrence, development and penetration process of the internal erosion in embankment dams [58].

4.3. Evolution with the Salinity

Permeability coefficient remains constant with the change of concentration. The results may be attributed to resulted from the rich silica content at low concentrations inhibits clay mineral swelling and dispersion. In addition, the scaly illite mineral mainly affects the permeability by reducing the effective seepage radius of the pores (see Figure 3b). We will estimate the thickness of the bound water layer on the surface of scaly illite by calculating the thickness of the electric double layer [23]. According to Equation (14), we estimate the Debye screening length χ_d (m) [59]:

$$\chi_d = \sqrt{\frac{\varepsilon_0 \varepsilon_r k_b T}{2000 N e^2 I_f}} \quad (14)$$

where $\varepsilon_0 = 8.854 \times 10^{-12}$ (F m⁻¹) is the electrical permittivity in vacuo, $\varepsilon_r = 78$ is the relative electrical permittivity, $k_b = 1.38 \times 10^{-23}$ (J K⁻¹) is the Boltzmann's constant, $T = 25$ °C = 298 (K) is the temperature, $N = 6.02 \times 10^{23}$ (mol⁻¹) is the Avogadro's constant, $e = 1.602 \times 10^{-19}$ (C) is the elementary charge, I_f (mol L⁻¹) is the ionic strength, when $C_f > 10^{-5}$ mol L⁻¹ and $5 < \text{pH} < 9$, the $I_f \approx C_f$ [27]. The value of the Debye screening length is 3.03×10^{-8} m at 0.0001 M salinity. In addition, we estimate the pore radius r (m) by Equation (15) [20]:

$$r = \sqrt{\frac{8k}{\phi}} \quad (15)$$

where k (m²) is the permeability, $\phi = 0.30$ is the porosity. The value of pore radius is 3.53×10^{-5} m at the same salinity. The thickness of the diffuse layer is approximately twice the Debye length [49], and the thickness of the stern layer is smaller than the thickness of the diffusion layer at low concentration. As $r \gg 2\chi_d$, the thickness of the electric double layer is negligible compared with the pore radius at 85% compaction. However, there will be different results at low salinity and low permeability. The liquid permeability of shaly sandstone increases with the increase in concentration, because the thickness of the bound water layer is important in the pore radius [24].

Low salinity has a dispersing effect on rich clay materials. The dispersive clay was used as filling materials in embankment dam projects. The structural safety of such dams has always been a major concern. The study of the streaming potential effect of dispersive clay at different salinities will be a significant problem, which will help the self-potential method to monitor the structural evolution of dams and make safety assessment and early warning.

5. Conclusions

In this study, SRM samples with different compactness and salinities were prepared. The variation law of the streaming potential phenomenon in the SRM is studied. We analyzed the dependence of the streaming potential coupling coefficient on compaction and concentration. The main conclusions are as follows:

- (1) When the content of clay in soil matrix is slight, the seepage follows Darcy's law. However, when the content of clay in soil matrix is rich, it is necessary to understand the seepage characteristics of SRM before the application of self-potential method. This will improve the measurement accuracy of the self-potential method.
- (2) The apparent streaming potential coupling coefficient is inversely proportional to the compactness. Different structures (compactness) of SRM have different streaming potential responses, which lays a foundation for the self-potential method to monitor the SRM structure. It is helpful to evaluate and predict the internal structural safety of dams.
- (3) The composition, morphology and the thickness of the bound water layer (electric double layer) of clay minerals determine the permeability of SRM in different salinities.

Further research on the streaming potential phenomenon of dispersive clay materials can expand the application range of the self-potential method.

Author Contributions: Methodology, M.Z. and K.W.; formal analysis, X.Z. and K.W.; data curation, X.Z.; writing—original draft preparation, X.Z.; writing—review and editing, K.W.; project administration, M.Z.; funding acquisition, M.Z. All authors have read and agreed to the published version of the manuscript.

Funding: This research was funded by National Natural Science Foundation of China, grant number 51879017, Chongqing Research Program of Basic Research and Frontier Technology, grant number cstc2017jcyjBX0066, Key Laboratory of Hydraulic and Waterway Engineering of the Ministry of Education, Chongqing Jiaotong University, grant number SLK2018B06 and The Graduate Education Innovative Fund Program of Chongqing Jiaotong University, grant number 2019B0102.

Institutional Review Board Statement: Not applicable.

Informed Consent Statement: Not applicable.

Data Availability Statement: Not applicable.

Acknowledgments: This research was funded by the National Natural Science Foundation of China (Grant No. 51879017), and Chongqing Research Program of Basic Research and Frontier Technology (Grant No. cstc2017jcyjBX0066), and Key Laboratory of Hydraulic and Waterway Engineering of the Ministry of Education, Chongqing Jiaotong University (Grant No. SLK2018B06), and Graduate Education Innovative Fund Program of Chongqing Jiaotong University (Grant no. 2019B0102). The authors appreciate all the institutions and individuals that have provided support for this paper.

Conflicts of Interest: The authors declare no conflict of interest.

References

1. Revil, A. Transport of water and ions in partially water-saturated porous media. Part 1. Constitutive equations. *Adv. Water Resour.* **2017**, *103*, 119–138. [[CrossRef](#)]
2. Zhou, Z.; Yang, H.; Wan, Z.H.; Liu, B.C. Computational model for electrical resistivity of soil-rock mixtures. *J. Mater. Civ. Eng.* **2016**, *28*, 06016009. [[CrossRef](#)]
3. Chen, T.; Yang, Y.; Zheng, H.; Wu, Z. Numerical determination of the effective permeability coefficient of soil-rock mixtures using the numerical manifold method. *Int. J. Numer. Anal. Methods Geomech.* **2019**, *43*, 381–414. [[CrossRef](#)]
4. Mao, D.; Revil, A.; Hort, R.D.; Munakata-Marr, J.; Atekwana, E.A.; Kulesa, B. Resistivity and self-potential tomography applied to groundwater remediation and contaminant plumes: Sandbox and field experiments. *J. Hydrol.* **2015**, *530*, 1–14. [[CrossRef](#)]
5. MacAllister, D.J.; Jackson, M.D.; Butler, A.P.; Vinogradov, J. Remote detection of saline intrusion in a coastal aquifer using borehole measurements of self-potential. *Water Resour. Res.* **2018**, *54*, 1669–1687. [[CrossRef](#)]
6. Zhu, Z.; Tao, C.; Shen, J.; Revil, A.; Deng, X.; Liao, S.; Yu, J. Self-Potential Tomography of a Deep-Sea Polymetallic Sulfide Deposit on Southwest Indian Ridge. *J. Geophys. Res.* **2020**, *125*, e2020JB019738. [[CrossRef](#)]
7. Von Smoluchowski, M. Contribution to the theory of electro-osmosis and related phenomena. *Bull. Int. Acad. Sci. Cracovie* **1903**, *3*, 184–199.
8. Hunter, R.J. *Zeta Potential in Colloid Science*; Academic Press: New York, NY, USA, 1981.
9. Pengra, D.B.; Li, S.X.; Wong, P.Z. Determination of rock properties by low-frequency AC electrokinetics. *J. Geophys. Res.* **1999**, *104*, 29485–29508. [[CrossRef](#)]
10. Guichet, X.; Jouniaux, L.; Pozzi, J.P. Streaming potential of a sand column in partial saturation conditions. *J. Geophys. Res.* **2003**, *108*, 2141. [[CrossRef](#)]
11. Morgan, F.D.; Williams, E.R.; Madden, T.R. Streaming potential properties of westerly granite with applications. *J. Geophys. Res.* **1989**, *94*, 12449–12461. [[CrossRef](#)]
12. Revil, A.; Saracco, G.; Labazuy, P. The volcano-electric effect. *J. Geophys. Res.* **2003**, *108*, 2251. [[CrossRef](#)]
13. Jaafar, M.Z.; Vinogradov, J.; Jackson, M.D. Measurement of streaming potential coupling coefficient in sandstones saturated with high salinity NaCl brine. *Geophys. Res. Lett.* **2009**, *36*, L21306. [[CrossRef](#)]
14. Vinogradov, J.; Jaafar, M.Z.; Jackson, M.D. Measurement of streaming potential coupling coefficient in sandstones saturated with natural and artificial brines at high salinity. *J. Geophys. Res.* **2010**, *115*, B12204. [[CrossRef](#)]
15. Walker, E.; Glover, P.W.J. Measurements of the relationship between microstructure, pH, and the streaming and zeta potentials of sandstones. *Transp. Porous Med.* **2017**, *121*, 183–206. [[CrossRef](#)] [[PubMed](#)]
16. Walker, E.; Glover, P.W.J.; Ruel, J. A transient method for measuring the DC streaming potential coefficient of porous and fractured rocks. *J. Geophys. Res.* **2014**, *119*, 957–970. [[CrossRef](#)]

17. Dukhin, A.; Dukhin, S.; Goetz, P. Electrokinetics at high ionic strength and hypothesis of the double layer with zero surface charge. *Langmuir* **2005**, *21*, 9990–9997. [[CrossRef](#)] [[PubMed](#)]
18. Alkafef, S.F.; Alajmi, A.F. The electrical conductivity and surface conduction of consolidated rock cores. *J. Colloid Interface Sci.* **2007**, *309*, 253–261. [[CrossRef](#)] [[PubMed](#)]
19. Tosha, T.; Matsushima, N.; Ishido, T. Zeta potential measured for an intact granite sample at temperatures to 200 °C. *Geophys. Res. Lett.* **2003**, *30*, 1295. [[CrossRef](#)]
20. Revil, A.; Cathles, L.M. Permeability of shaly sands. *Water Resour. Res.* **1999**, *35*, 651–662. [[CrossRef](#)]
21. Rowlands, W.N.; O'Brien, R.W.; Hunter, R.J.; Patrick, V. Surface properties of aluminum hydroxide at high salt concentration. *J. Colloid Interface Sci.* **1997**, *188*, 325–335. [[CrossRef](#)]
22. Jougnot, D.; Mendieta, A.; Leroy, P.; Maineult, A. Exploring the effect of the pore size distribution on the streaming potential generation in saturated porous media, insight from pore network simulations. *J. Geophys. Res.* **2019**, *124*, 5315–5335. [[CrossRef](#)]
23. Dang, F.; Liu, H.W.; Wang, X.W.; Xue, H.B.; Ma, Z.Y. Empirical formulas of permeability of clay based on effective pore ratio. *Chin. J. Rock. Mech. Eng.* **2015**, *34*, 1909–1917. [[CrossRef](#)]
24. Wang, L.; Mao, Z.Q.; Sun, Z.C.; Luo, X.P.; Song, Y.; Wang, Z.L. A new method for calculating fluid permeability of shaly sandstone. *Chin. J. Geophys.* **2015**, *58*, 3837–3844. [[CrossRef](#)]
25. Jouniaux, L.; Pozzi, J.P. Permeability dependence of streaming potential in rocks for various fluid conductivities. *Geophys. Res. Lett.* **1995**, *22*, 485–488. [[CrossRef](#)]
26. Jouniaux, L.; Pozzi, J.P. Streaming potential and permeability of saturated sandstones under triaxial stress: Consequences for electrotelluric anomalies prior to earthquakes. *J. Geophys. Res.* **1995**, *100*, 10197–10209. [[CrossRef](#)]
27. Glover, P.W.J.; Déry, N. Streaming potential coupling coefficient of quartz glass bead packs: Dependence on grain diameter, pore size, and pore throat radius. *Geophysics* **2010**, *75*, F225–F241. [[CrossRef](#)]
28. Glover, P.W.J. Modelling pH-dependent and microstructure-dependent streaming potential coefficient and zeta potential of porous sandstones. *Transp. Porous Med.* **2018**, *124*, 31–56. [[CrossRef](#)]
29. Revil, A.; Leroy, P. Constitutive equations for ionic transport in porous shales. *J. Geophys. Res.* **2004**, *109*, B03208. [[CrossRef](#)]
30. Revil, A.; Jardani, A. *The Self-Potential Method: Theory and Applications in Environmental Geosciences*; Cambridge University Press: Cambridge, UK, 2013.
31. Jougnot, D.; Roubinet, D.; Guarracino, L.; Maineult, A. Modeling streaming potential in porous and fractured media, description and benefits of the effective excess charge density approach. In *Advances in Modeling and Interpretation in Near Surface Geophysics*; Springer: Cham, Switzerland, 2020; pp. 61–96.
32. Guarracino, L.; Jougnot, D. A physically based analytical model to describe effective excess charge for streaming potential generation in water saturated porous media. *J. Geophys. Res.* **2018**, *123*, 52–65. [[CrossRef](#)]
33. Cheng, Q.; Tao, M.; Chen, X.; Binley, A. Evaluation of electrical resistivity tomography (ERT) for mapping the soil–rock interface in karstic environments. *Environ. Earth Sci.* **2019**, *78*, 1–14. [[CrossRef](#)]
34. De Carlo, L.; Caputo, M.C.; Masciale, R.; Vurro, M.; Portoghese, I. Monitoring the Drainage Efficiency of Infiltration Trenches in Fractured and Karstified Limestone via Time-Lapse Hydrogeophysical Approach. *Water* **2020**, *12*, 2009. [[CrossRef](#)]
35. Brindt, N.; Rahav, M.; Wallach, R. ERT and salinity—A method to determine whether ERT-detected preferential pathways in brackish water-irrigated soils are water-induced or an artifact of salinity. *J. Hydrol.* **2019**, *574*, 35–45. [[CrossRef](#)]
36. Ikard, S.J.; Revil, A.; Jardani, A.; Woodruff, W.F.; Parekh, M.; Mooney, M. Saline pulse test monitoring with the self-potential method to nonintrusively determine the velocity of the pore water in leaking areas of earth dams and embankments. *Water Resour. Res.* **2012**, *48*, W04201. [[CrossRef](#)]
37. Jougnot, D.; Linde, N.; Haarder, E.B.; Looms, M.C. Monitoring of saline tracer movement with vertically distributed self-potential measurements at the HOBE agricultural test site, Voulund, Denmark. *J. Hydrol.* **2015**, *521*, 314–327. [[CrossRef](#)]
38. Panthulu, T.V.; Krishnaiah, C.; Shirke, J.M. Detection of seepage paths in earth dams using self-potential and electrical resistivity methods. *Eng. Geol.* **2001**, *59*, 281–295. [[CrossRef](#)]
39. Sheffer, M.R.; Oldenburg, D.W. Three-dimensional modelling of streaming potential. *Geophys. J. Int.* **2007**, *169*, 839–848. [[CrossRef](#)]
40. Bolève, A.; Janod, F.; Revil, A.; Lafon, A.; Fry, J.J. Localization and quantification of leakages in dams using time-lapse self-potential measurements associated with salt tracer injection. *J. Hydrol.* **2011**, *403*, 242–252. [[CrossRef](#)]
41. Soueid Ahmed, A.; Revil, A.; Bolève, A.; Steck, B.; Vergniault, C.; Courivaud, J.R.; Jougnot, D.; Abbas, M. Determination of the permeability of seepage flow paths in dams from self-potential measurements. *Eng. Geol.* **2020**, *268*, 105514. [[CrossRef](#)]
42. Soueid Ahmed, A.; Revil, A.; Steck, B.; Vergniault, C.; Jardani, A.; Vincelas, G. Self-potential signals associated with localized leaks in embankment dams and dikes. *Eng. Geol.* **2019**, *253*, 229–239. [[CrossRef](#)]
43. Qiu, Z.F.; Wang, J.J. Experimental study on the anisotropic hydraulic conductivity of a sandstone–mudstone particle mixture. *J. Hydrol. Eng.* **2015**, *20*, 04015029. [[CrossRef](#)]
44. Jougnot, D.; Linde, N. Self-potentials in partially saturated media: The importance of explicit modeling of electrode effects. *Vadose Zone J.* **2013**, *12*. [[CrossRef](#)]
45. Zhou, Z.; Yang, H.; Wang, X.; Liu, B. Model development and experimental verification for permeability coefficient of soil-rock mixture. *Int. J. Geomech.* **2017**, *17*, 04016106. [[CrossRef](#)]
46. Bear, J. *Dynamics of Fluid in Porous Media*; Elsevier: New York, NY, USA, 1972.

47. Liu, X.R.; Tu, Y.L.; Wang, P.; Zhong, Z.L.; Tang, W.B.; Du, L.B. Particle breakage of soil-rock aggregate based on large-scale direct shear tests. *Chin. J. Geotech. Eng.* **2017**, *39*, 1425–1434. [[CrossRef](#)]
48. Bolève, A.; Crespy, A.; Revil, A.; Janod, F.; Mattiuzzo, J.L. Streaming potentials of granular media: Influence of the Dukhin and Reynolds numbers. *J. Geophys. Res.* **2007**, *112*, B08204. [[CrossRef](#)]
49. Revil, A.; Schwaeger, H.; Cathless, L.M.; Manhardt, P.D. Streaming potential in porous media 2. Theory and application to geothermal systems. *J. Geophys. Res.* **1999**, *104*, 20033–20048. [[CrossRef](#)]
50. Phillips, S.L.; Ozbek, H.; Otto, R.J. Basic energy properties of electrolytic solutions database. In Proceedings of the Sixth International CODATA Conference, Palermo, Italy, 22 May 1978.
51. Glover, P.W.J.; Walker, E.; Jackson, M.D. Streaming-potential coefficient of reservoir rock: A theoretical model. *Geophysics* **2012**, *77*, D17–D43. [[CrossRef](#)]
52. Winsauer, W.O.; Shearin, H.M.; Masson, P.H.; Williams, M. Resistivity of brine-saturated sands in relation to pore geometry. *AAPG Bull.* **1952**, *36*, 253–277.
53. Tyler, S.W.; Wheatcraft, S.W. Fractal processes in soil water retention. *Water Resour. Res.* **1990**, *26*, 1047–1054. [[CrossRef](#)]
54. Wang, Y.; Li, X.; Zheng, B.; Mao, T.Q.; Hu, R.L. Investigation of the effect of soil matrix on flow characteristics for soil and rock mixture. *Géotech. Lett.* **2016**, *6*, 1–8. [[CrossRef](#)]
55. Lorne, B.; Perrier, F.; Avouac, J.-P. Streaming potential measurements 1. properties of the electrical double layer from crushed rock samples. *J. Geophys. Res.* **1999**, *104*, 17857–17877. [[CrossRef](#)]
56. Watanabe, T.; Katagishi, Y. Deviation of linear relation between streaming potential and pore fluid pressure difference in granular material at relatively high Reynolds numbers. *Earth Planets Space* **2006**, *58*, 1045–1051. [[CrossRef](#)]
57. Kuwano, O.; Nakatani, M.; Yoshida, S. Effect of the flow state on streaming current. *Geophys. Res. Lett.* **2006**, *33*, L21309. [[CrossRef](#)]
58. Van Beek, V.M.; Van Essen, H.M.; Vandenboer, K.; Bezuijen, A. Developments in modelling of backward erosion piping. *Géotechnique* **2015**, *65*, 740–754. [[CrossRef](#)]
59. Revil, A.; Pezard, P.A.; Glover, P.W.J. Streaming potential in porous media. I. Theory of the zeta-potential. *J. Geophys. Res.* **1999**, *104*, 20021–20031. [[CrossRef](#)]